





Magnetic hedgehog lattices in noncentrosymmetric metals

Shun Okumura , Satoru Hayami , Yasuyuki Kato , and Yukitoshi Motome 

Department of Applied Physics, The University of Tokyo, Tokyo 113-8656, Japan



(Received 5 August 2019; revised manuscript received 10 March 2020; accepted 11 March 2020; published 13 April 2020)

The magnetic hedgehog lattice (HL) is a noncoplanar magnetic texture with a periodic array of magnetic monopoles and antimonopoles. Despite phenomenological and numerical studies thus far, there remain open issues on the microscopic origin, especially with respect to the recent experimental findings of two different types of HLs even at zero magnetic field. Here, we study the stability of the HLs for an effective spin model with long-range interactions arising from the itinerant nature of electrons. By variational calculations and simulated annealing, we find that the HLs are stabilized in the ground state at zero magnetic field by the synergetic effect of the antisymmetric exchange interactions generated by the spin-orbit coupling and the multiple-spin interactions generated by the spin-charge coupling. We also clarify the phase diagram in the magnetic fields, which includes topological phase transitions with pair annihilation of the monopoles and antimonopoles depending on the field directions.

DOI: [10.1103/PhysRevB.101.144416](https://doi.org/10.1103/PhysRevB.101.144416)

I. INTRODUCTION

Chirality, often termed as handedness, is a key concept in a broad field of science, ranging from particle physics to biology. In condensed matter physics, chiral magnetic textures, which break both inversion and mirror symmetries in addition to time-reversal symmetry, have recently attracted considerable attention for potential applications to next-generation electronic devices. There are a variety of chiral magnetic textures, such as skyrmion lattices [1] and chiral soliton lattices [2]. Noncollinear and noncoplanar spin arrangements in these textures generate emergent electromagnetic fields through the Berry phase mechanism, which induce unconventional transport, optical, and magnetoelectric properties [3–5].

Recently, a three-dimensional chiral magnetic texture, which is called the hedgehog lattice (HL), was discovered in the $B20$ -type compound MnGe [6,7]. The magnetic structure is characterized by cubic three wave vectors, and hence it is referred to as the triple- Q hedgehog lattice ($3Q$ -HL) [Fig. 1(b)]. The $3Q$ -HL has a periodic array of hyperbolic hedgehog and antihedgehog spin textures, which generates an emergent magnetic field with a periodic array of radial hedgehogs and antihedgehogs regarded as magnetic monopoles and antimonopoles, as shown in Fig. 1(c) [8–10]. The peculiar magnetic field was discussed as a source of the enormous topological Hall effect [11] and thermoelectric effect [12,13]. In addition, by a substitution of Ge by Si, the $3Q$ -HL changes into a different HL characterized by tetrahedral four wave vectors, dubbed the quadruple- Q hedgehog lattice ($4Q$ -HL) [Fig. 1(a)] [14]. Remarkably, the magnetic periods of these $3Q$ - and $4Q$ -HLs are very short, ~ 2 – 3 nm, in contrast to most of the skyrmion lattices.

Such magnetic HLs have been theoretically studied prior to the experimental discovery, e.g., by the Ginzburg-Landau theory [15], variational calculations [16], and Monte Carlo (MC) simulations [17]. The variational study for a classical

spin model showed that the $3Q$ -HL is not stabilized, whereas the $4Q$ -HL is obtained in an applied magnetic field [16]. The $4Q$ -HL in a field was also confirmed by MC simulations [17]. The previous studies, however, do not predict the stable HLs in the absence of magnetic fields, contradicting the experimental observations. Furthermore, to account for the short-period twist, the localized spin picture requires a large Dzyaloshinskii-Moriya (DM) interaction [18,19], but it was estimated to be very weak [20–22]. Indeed, recent analyses based on first-principles calculations showed that the stable HLs are not obtained by two spin interactions including the DM interaction [23]. The importance of four- and six-spin interactions including spin chirality was also proposed [24,25].

In this paper, we study the stability of $4Q$ - and $3Q$ -HLs from a different viewpoint from the previous studies, by taking into account the itinerant nature of electrons. We consider an effective model with long-range exchange interactions originating from the coupling between charge, spin, and orbital degrees of freedom. By variational calculations and simulated annealing, we show that the model realizes both $4Q$ - and $3Q$ -HLs at zero field, through the cooperation between the DM-type asymmetric exchange interaction arising from the spin-orbit coupling and the multiple-spin interactions from the spin-charge coupling. We also study the effect of an applied magnetic field on these HLs. Depending on the field directions, we find that the system exhibits multiple phase transitions while changing from the $4Q$ - and $3Q$ -HLs to the forced ferromagnetic (FFM) state. Notably, we show that some of them are topological phase transitions with pair annihilation of the monopoles and antimonopoles. We demonstrate how the pair annihilation takes place by tracing the positions of the monopoles and antimonopoles.

The rest of the paper is organized as follows. In Sec. II, we introduce the effective spin model derived from an itinerant electron model. In Sec. III, we describe the methods that

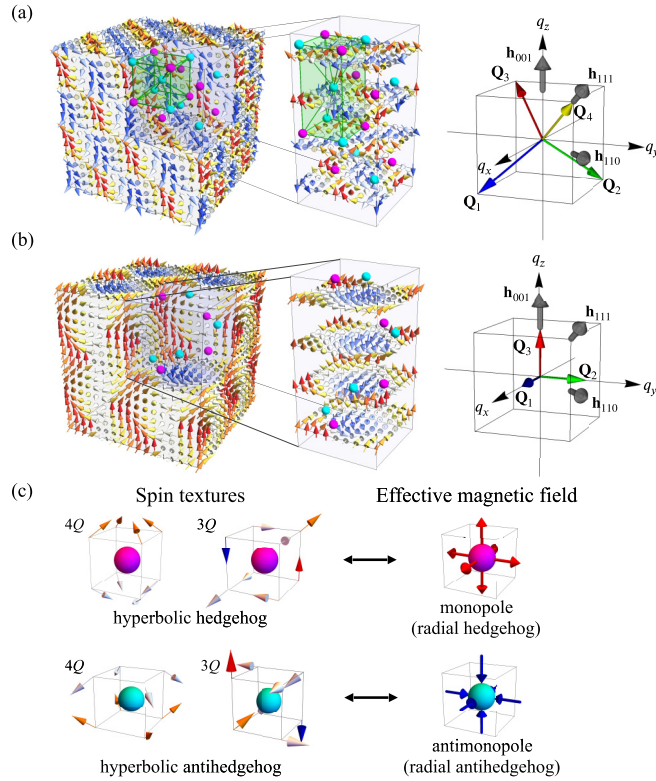


FIG. 1. Spin textures of (a) $4Q$ and (b) $3Q$ hedgehog lattices obtained by simulated annealing for the model in Eq. (2). The enlarged pictures display the magnetic unit cell with the spin configurations on every two $[001]$ layers for clarity. The magenta (cyan) balls represent the (anti)monopoles at the (anti)hedgehog cores, which locate at the interstitial positions of the cubic lattice sites. In (a), there are eight monopoles and eight antimonopoles in the magnetic unit cell, forming two interpenetrating body-centered-cubic lattices (one of them is shown by the green guides). Meanwhile, there are four monopoles and four antimonopoles in (b), which comprise spirals running in the $[100]$, $[010]$, and $[001]$ directions. The right panels show the ordering vectors for the (a) $4Q$ and (b) $3Q$ cases. The thick arrows (gray) represent the directions of the magnetic field along the $[001]$, $[110]$, and $[111]$ axes. (c) Correspondences between the spin textures and the effective magnetic fields. The cube represents the lattice unit composed of the eight lattice sites surrounding a monopole and an antimonopole.

we use in this paper to investigate the ground state of the effective spin model. In Sec. IV, we show the phase diagram at zero field including the HLs. In Sec. V, we show the phase diagram in magnetic fields applied in three symmetric directions. In Sec. VI, we discuss field-induced topological phase transitions caused by pair annihilation of monopoles and antimonopoles. Section VII is devoted to the summary.

II. MODEL

In this section, we present the model which we use in the present paper. Starting from an itinerant electron model with spin-charge and spin-orbit couplings in Sec. II A, we discuss the effective model with long-ranged exchange interactions induced by the itinerant nature of electrons in Sec. II B.

A. Itinerant electron model

In order to investigate the microscopic origin of magnetic HLs, we begin with a minimal model including itinerant electrons, an extended Kondo lattice model that describes the coupling between the itinerant electron spins and localized magnetic moments. While the Kondo lattice model has been studied for f electron systems, where the f electrons comprise the localized moments [26,27], we note that it is also regarded as an effective model for the Hubbard-type models, which have been used widely, e.g., for d electron systems, at the level of the mean-field approximation [28]. In the current paper, we include an antisymmetric spin-orbit coupling arising from spatial inversion symmetry breaking in noncentrosymmetric systems. The Hamiltonian in the wave-number representation is given by

$$\mathcal{H} = \sum_{\mathbf{k}\sigma} (\varepsilon_{\mathbf{k}} - \mu) c_{\mathbf{k}\sigma}^\dagger c_{\mathbf{k}\sigma} + J_K \sum_{\mathbf{k}\mathbf{q}\sigma\sigma'} c_{\mathbf{k}\sigma}^\dagger \sigma_{\sigma\sigma'} c_{\mathbf{k}+\mathbf{q}\sigma'} \cdot \mathbf{S}_{\mathbf{q}} + \sum_{\mathbf{k}\sigma\sigma'} \mathbf{g}_{\mathbf{k}} \cdot c_{\mathbf{k}\sigma}^\dagger \sigma_{\sigma\sigma'} c_{\mathbf{k}\sigma'}, \quad (1)$$

where $c_{\mathbf{k}\sigma}^\dagger$ ($c_{\mathbf{k}\sigma}$) is a creation (annihilation) operator of an itinerant electron with wave vector \mathbf{k} and spin $\sigma = \uparrow$ or \downarrow . The first term describes the kinetic energy of itinerant electrons; $\varepsilon_{\mathbf{k}}$ is the energy dispersion and μ is the chemical potential. The second term is for the Kondo coupling between itinerant electron spins and localized spin moments; $\boldsymbol{\sigma} = (\sigma^x, \sigma^y, \sigma^z)$ is the vector of Pauli matrices, and $\mathbf{S}_{\mathbf{q}} = \frac{1}{\sqrt{N}} \sum_l \mathbf{S}_{\mathbf{r}_l} e^{-i\mathbf{q}\cdot\mathbf{r}_l}$ is the Fourier transform of a localized moment $\mathbf{S}_{\mathbf{r}_l} = (S_{\mathbf{r}_l}^x, S_{\mathbf{r}_l}^y, S_{\mathbf{r}_l}^z)$ defined at site l , where N is the number of lattice sites. For simplicity, $\mathbf{S}_{\mathbf{r}_l}$ is regarded as a classical spin with the length $|\mathbf{S}_{\mathbf{r}_l}| = 1$. J_K is the exchange coupling constant the sign of which is irrelevant for the classical spins. The last term represents the antisymmetric spin-orbit coupling induced by spatial inversion symmetry breaking; $\mathbf{g}_{\mathbf{k}} = (g_{\mathbf{k}}^x, g_{\mathbf{k}}^y, g_{\mathbf{k}}^z)$ is called the g vector, which plays an important role in chiral magnets. In the following, we consider the model on a simple cubic lattice with the lattice constant being unity for simplicity; noncentrosymmetric nature is effectively taken into account in the g vector $\mathbf{g}_{\mathbf{k}}$ with an odd function of \mathbf{k} .

B. Effective spin model

In general, the coupling between itinerant electrons and localized spins generates effective exchange interactions between the localized spins. For instance, in the strong-coupling case with $J_K \gg |\varepsilon_{\mathbf{k}} - \mu|$, an effective ferromagnetic interaction is generated to maximize the kinetic energy of itinerant electrons by aligning neighboring spins, which is called the double-exchange interaction [29,30]. On the other hand, in the weak-coupling case with $J_K \ll |\varepsilon_{\mathbf{k}} - \mu|$, the effective magnetic interaction becomes long ranged and oscillating in space, which is called the Ruderman-Kittel-Kasuya-Yosida (RKKY) interaction [31–33]. In this paper, we consider the weak-coupling case of the model in Eq. (1) by an effective spin model derived by perturbation expansion in terms of J_K . Our model includes a higher-order effect of the spin-charge coupling beyond the RKKY interaction discussed in the previous studies [34–36], and also a DM-type interaction

originating from the spin-orbit coupling in the last term in Eq. (1) [37]. The Hamiltonian reads

$$\mathcal{H} = \sum_{\eta} \left[-J\mathbf{S}_{\mathbf{Q}_{\eta}} \cdot \mathbf{S}_{-\mathbf{Q}_{\eta}} + \frac{K}{N}(\mathbf{S}_{\mathbf{Q}_{\eta}} \cdot \mathbf{S}_{-\mathbf{Q}_{\eta}})^2 - i\mathbf{D}_{\eta} \cdot \mathbf{S}_{\mathbf{Q}_{\eta}} \times \mathbf{S}_{-\mathbf{Q}_{\eta}} \right] - \sum_l \mathbf{h} \cdot \mathbf{S}_{\mathbf{r}_l}. \quad (2)$$

The first term denotes the RKKY interaction, which is derived by the second-order perturbation with respect to J_K [31–33]. In general, this tends to stabilize a spiral magnetic texture. The second term is the biquadratic interaction, which is most relevant among the higher-order perturbations with respect to J_K [36]. Hereafter, we consider the positive coupling constant $K > 0$, which is known to prefer noncollinear and noncoplanar spin configurations [34–36]. The third term represents a DM-type interaction arising from the antisymmetric spin-orbit coupling, which is derived by the second-order perturbation with respect to J_K [37]. This also brings a twist in spin textures, and plays a role in not only choosing the chirality but also giving an anisotropy in spin space. Note that we ignore other anisotropic exchange interactions originating from the antisymmetric spin-orbit coupling, for simplicity [37]. The last term describes the Zeeman coupling to an external magnetic field \mathbf{h} .

In Eq. (2), all the exchange interactions are long ranged in real space and specified by particular wave numbers \mathbf{Q}_{η} . This inherits the itinerant nature of electrons; specifically, the wave vectors \mathbf{Q}_{η} are set by the multiple maxima in the spin-dependent bare susceptibility of itinerant electrons [35,36]. Corresponding to the 3 Q - and 4 Q -HLs, we assume two sets of \mathbf{Q}_{η} : One is a set of the tetrahedral wave vectors as $\mathbf{Q}_1 = (Q, -Q, -Q)$, $\mathbf{Q}_2 = (-Q, Q, -Q)$, $\mathbf{Q}_3 = (-Q, -Q, Q)$, and $\mathbf{Q}_4 = (Q, Q, Q)$ [Fig. 1(a)], and the other is a set of the cubic wave vectors as $\mathbf{Q}_1 = (Q, 0, 0)$, $\mathbf{Q}_2 = (0, Q, 0)$, and $\mathbf{Q}_3 = (0, 0, Q)$, which are orthogonal to each other [Fig. 1(b)]. In the following calculations, we set $Q = \pi/4$ (period of eight lattice sites); we confirm that the following results remain qualitatively the same for different choices of Q . Although the direction of \mathbf{D}_{η} is independent of that of \mathbf{Q}_{η} in general, we assume $\mathbf{D}_{\eta} \parallel \mathbf{Q}_{\eta}$ that stabilizes proper-screw-type spin textures [38]. We note that the HLs can be composed of superpositions of the proper screws. The magnetic field \mathbf{h} is applied along the [001], [110], and [111] directions as shown in the right panels of Figs. 1(a) and 1(b). We set the energy scale as $J = 1$. We consider the system with $N = 16^3$ spins under periodic boundary conditions. We confirmed that the following results remain the same for $N = 24^3$ spins (not shown here).

III. METHOD

In this section, we present the methods to study the ground state of the model in Eq. (2). At zero magnetic field, we mainly adopt variational calculations by comparing the energy of several different spin states, as introduced in Sec. III A. In addition, we use simulated annealing, which is introduced in Sec. III B, not only to confirm the variational results but also to study the ground state in an applied magnetic field where it is difficult to infer the variational states.

A. Variational calculations

In the variational calculations, we consider the following spin textures as the variational states at zero magnetic field. The simplest one is given by

$$\mathbf{S}_{\mathbf{r}_l} \propto \sum_{\eta=1}^n \hat{\mathbf{a}}_{\eta} \cos Q_{\eta l}, \quad (3)$$

where $\hat{\mathbf{a}}_{\eta}$ is the unit vector parallel to \mathbf{Q}_{η} and $Q_{\eta l} = \mathbf{Q}_{\eta} \cdot \mathbf{r}_l + \varphi_{\eta}$ (φ_{η} represents the phase shift); $n = 1, 2, 3$ for the 3 Q case and $n = 1, 2, 3, 4$ for the 4 Q case. This is a set of nonchiral states that has no energy gain from the DM-type interaction. Another variational state is a chiral one described as the equal superpositions of proper screws:

$$\mathbf{S}_{\mathbf{r}_l} \propto \sum_{\eta=1}^n (\hat{\mathbf{b}}_{\eta} \sin Q_{\eta l} + \hat{\mathbf{c}}_{\eta} \cos Q_{\eta l}), \quad (4)$$

where $\hat{\mathbf{b}}_{\eta}$ and $\hat{\mathbf{c}}_{\eta}$ are the unit vectors orthogonal to $\hat{\mathbf{a}}_{\eta}$ and each other ($\hat{\mathbf{a}}_{\eta}$, $\hat{\mathbf{b}}_{\eta}$, and $\hat{\mathbf{c}}_{\eta}$ form a right-handed system). Note that the $n = 3$ ($n = 4$) state for 3 Q (4 Q) corresponds to the 3 Q (4 Q)-HL shown in Fig. 1(a) [1(b)]. In addition, we include another variational state called the double- Q chiral stripe (2 Q -CS) found in the previous study [39]:

$$\mathbf{S}_{\mathbf{r}_l} \propto \sqrt{1-u^2} \hat{\mathbf{b}}_1 \sin Q_{1l} + \sqrt{1-u^2} \hat{\mathbf{c}}_1 \cos Q_{1l} + u \hat{\mathbf{a}}_1, \quad (5)$$

where $u = v \sin Q_{2l}$. In the variational calculations, we compare the energy for all the variational states by varying φ_{η} from zero to Q and v from zero to 1 to find the lowest-energy candidate for the ground state.

B. Simulated annealing

In the simulated annealing, we numerically find the candidate for the ground state by means of MC simulation. We gradually reduce the temperature of the system from $T = 1$ to 10^{-5} with a condition $T_n = 10^{-0.1n}$, where T_n is the temperature in the n th step. During the annealing, we spend a total of 10^5 – 10^6 MC sweeps by using the standard Metropolis algorithm. After annealing at a particular value of the field strength $h = |\mathbf{h}|$, we increase or decrease h successively by $\Delta h = 0.01$. At every shift by Δh , we heat the system up to $T = 10^{-3}$ and cool down again to $T = 10^{-5}$ by annealing. Carefully comparing the energy by starting from various values of h , we map out the magnetic phase diagram.

For the state obtained by the simulated annealing, we calculate the magnetization per site along the field direction:

$$m = \frac{1}{N} \sum_l \mathbf{S}_{\mathbf{r}_l} \cdot \hat{\mathbf{h}}, \quad (6)$$

where $\hat{\mathbf{h}}$ is the unit vector in the field direction, and the magnetic susceptibility

$$\chi = \frac{m(h + \Delta h) - m(h)}{\Delta h}. \quad (7)$$

To identify the multiple- Q magnetic orders, we also calculate the magnetic moment with wave vector \mathbf{q} :

$$m_{\mathbf{q}} = \sqrt{\frac{S(\mathbf{q})}{N}}, \quad (8)$$

where $S(\mathbf{q})$ is the spin structure factor defined by

$$S(\mathbf{q}) = \frac{1}{N} \sum_{l,l'} \mathbf{S}_{\mathbf{r}_l} \cdot \mathbf{S}_{\mathbf{r}_{l'}} e^{-i\mathbf{q} \cdot (\mathbf{r}_l - \mathbf{r}_{l'})}. \quad (9)$$

In addition, following Ref. [17], we define the monopole charge in each unit cube by using the fluxes $\mathbf{\Omega}_p$ penetrating six square plaquettes of the cube as [40]

$$Q_m(\mathbf{r}_c) = \frac{1}{4\pi} \sum_{p \in \text{unit cube}} \mathbf{\Omega}_p \cdot \hat{\mathbf{n}}_p, \quad (10)$$

where \mathbf{r}_c is the center position of the unit cube and $\hat{\mathbf{n}}_p$ is the normal unit vector of the p th plaquette pointing outward of the cube. We compute the flux $\mathbf{\Omega}_p$ by dividing the p th plaquette into two triangles and taking the sum of the solid angles of three spins on the two triangles $i = 1$ and 2. Each solid angle is calculated by

$$\Omega_i = 2 \tan^{-1} \left\{ \frac{\mathbf{S}_1 \cdot (\mathbf{S}_2 \times \mathbf{S}_3)}{1 + \mathbf{S}_1 \cdot \mathbf{S}_2 + \mathbf{S}_2 \cdot \mathbf{S}_3 + \mathbf{S}_3 \cdot \mathbf{S}_1} \right\}, \quad (11)$$

where \mathbf{S}_1 , \mathbf{S}_2 , and \mathbf{S}_3 are the three spins on the i th triangle in the clockwise order viewed from the center of the cube, and the sign of Ω_i is taken to be the same as that of $\mathbf{S}_1 \cdot (\mathbf{S}_2 \times \mathbf{S}_3)$: $\Omega_i \in [-2\pi, 2\pi)$. The flux $\mathbf{\Omega}_p$ is defined as a perpendicular vector to the p th plaquette as

$$\mathbf{\Omega}_p = \sum_{i \in p} \Omega_i \hat{\mathbf{n}}_p. \quad (12)$$

By substituting Eq. (12) into Eq. (10), we obtain the monopole charge $Q_m(\mathbf{r}_c)$. This quantity detects the monopoles and antimonopoles as it takes the value of +1 (−1) when a monopole (antimonopole) exists in the unit cube. The monopoles and antimonopoles are connected by flows of the flux $\mathbf{\Omega}_p$ in Eq. (12). We compute the total number of monopoles and antimonopoles in the magnetic unit cell, N_m , as

$$N_m = \sum_{\mathbf{r}_c \in V_m} |Q_m(\mathbf{r}_c)|, \quad (13)$$

where V_m is the magnetic unit cell (8^3 sites in the following calculations). We also measure the distances between the monopoles and antimonopoles by using \mathbf{r}_c where $Q_m(\mathbf{r}_c) = \pm 1$. In particular, we compute the minimum distance between the monopoles and antimonopoles by

$$d_m = \min |\mathbf{r}_c^m - \mathbf{r}_c^a|, \quad (14)$$

where \mathbf{r}_c^m and \mathbf{r}_c^a denote \mathbf{r}_c for the monopoles and antimonopoles. This is an important quantity for not only monitoring topological phase transitions by pair annihilation between monopoles and antimonopoles but also understanding the behavior of the net scalar spin chirality introduced below. We note, however, that $\mathbf{r}_c^{m(a)}$ gives an approximate position of the (anti)monopole core within an accuracy of the lattice constant, and d_m changes discontinuously by definition.

Finally, we calculate the net scalar spin chirality which gives rise to the topological Hall effect in itinerant electron systems [41]. We define the local scalar spin chirality at each lattice site \mathbf{r}_l by the sum of spin triple products on four

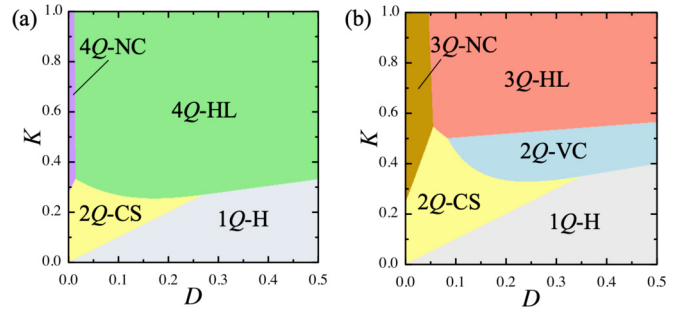


FIG. 2. Phase diagrams of the model in Eq. (2) at zero field for the (a) 4Q and (b) 3Q cases. 4Q(3Q)-HL, 4Q(3Q)-NC, 2Q-VC, 2Q-CS, and 1Q-H represent the chiral 4Q (3Q) hedgehog lattice, the nonchiral 4Q (3Q), the 2Q vortex crystal, the 2Q chiral stripe, and the 1Q helical states, respectively.

triangles on the $\alpha\beta$ plane ($\alpha, \beta = x, y, z$) as [40]

$$\chi_{sc}^\gamma(\mathbf{r}_l) = \frac{1}{2} \sum_{\alpha\beta\nu_\alpha\nu_\beta} \epsilon^{\alpha\beta\gamma} \nu_\alpha \nu_\beta \mathbf{S}_{\mathbf{r}_l} \cdot (\mathbf{S}_{\mathbf{r}_l + \nu_\alpha \hat{\delta}_\alpha} \times \mathbf{S}_{\mathbf{r}_l + \nu_\beta \hat{\delta}_\beta}), \quad (15)$$

where γ is the perpendicular direction to the $\alpha\beta$ plane, $\epsilon^{\alpha\beta\gamma}$ is the Levi-Civita symbol, $\nu_{\alpha(\beta)} = \pm 1$, and $\hat{\delta}_{\alpha(\beta)}$ is the unit translation vector in the $\alpha(\beta)$ direction. By taking the sum over all the sites and three planes, we obtain the net scalar spin chirality:

$$\chi_{sc} = \frac{1}{N} \sum_{\gamma l} \chi_{sc}^\gamma(\mathbf{r}_l). \quad (16)$$

Since Eqs. (11) and (15) share the spin triple products, χ_{sc} is related with the (oriented) summation of the flux $\mathbf{\Omega}_p$ in Eq. (12). As mentioned above, the flows of the flux connect the monopoles and antimonopoles, and hence the lengths of the flux flows, which are approximately given by the distances $|\mathbf{r}_c^m - \mathbf{r}_c^a|$, affect χ_{sc} . We will discuss such a relation in Sec. VI.

IV. PHASE DIAGRAM AT ZERO FIELD

First, we show the results in the absence of the magnetic field obtained by the variational calculations in Sec. III A. Figures 2(a) and 2(b) display the magnetic phase diagrams for the 4Q and 3Q cases, respectively, while varying $D = |\mathbf{D}_\eta|$ and K in Eq. (2). When $K = 0$, a nonzero D stabilizes the chiral 1Q helical state (1Q-H), which remains stable in the small K region for $D > 0$ in both 4Q and 3Q cases. On the other hand, when introducing K with $D = 0$, the 2Q-CS is stabilized in both cases, but replaced by the nonchiral 4Q and 3Q states in the larger K region. A similar sequence of the phase transitions was found in two dimensions [36,39]. When D and K are both relevant, however, we find the 4Q- and 3Q-HLs in the wide parameter range, in addition to a chiral 2Q state in the 3Q case, which is a Bloch-type vortex crystal (2Q-VC) [37]. We confirm the stability of these HLs also by the simulated annealing in Sec. III B; typical spin configurations for the 4Q- and 3Q-HLs are presented in Figs. 1(a) and 1(b), respectively.

Thus, our results indicate that the 4Q- and 3Q-HLs are stabilized by cooperation between the RKKY interaction,

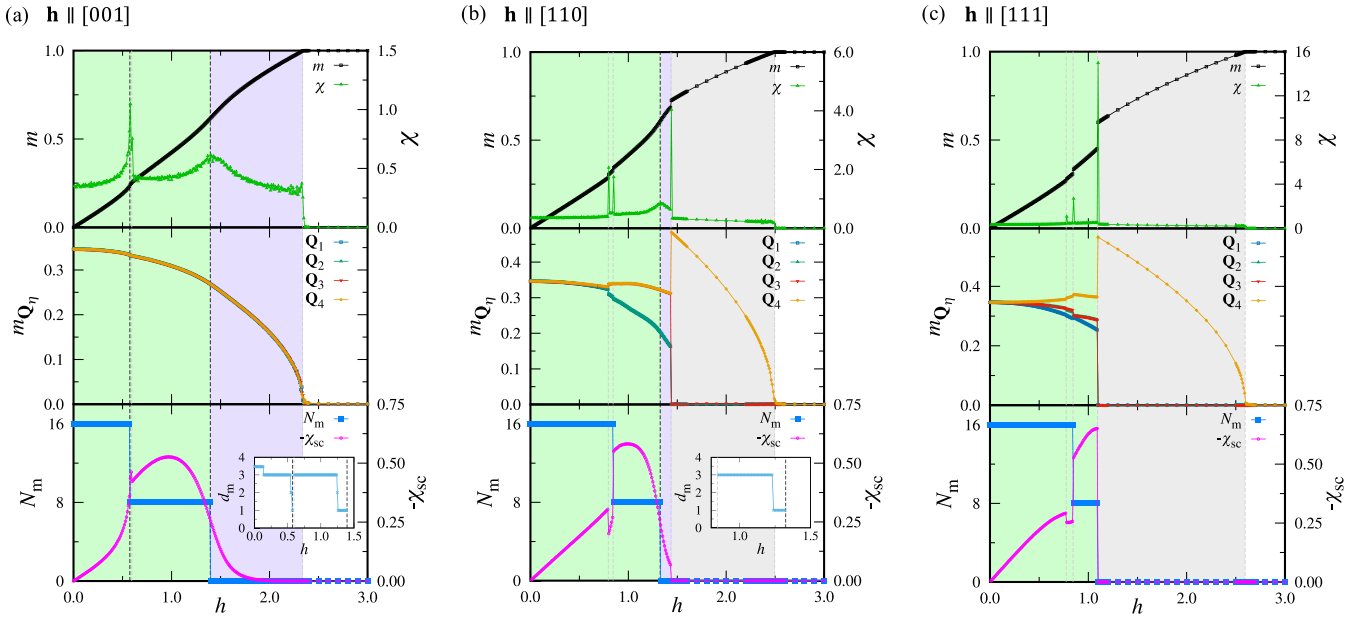


FIG. 3. Phase transitions in the magnetic fields along the (a) [001], (b) [110], and (c) [111] directions in the $4Q$ case: the magnetization m in Eq. (6); the magnetic susceptibility χ in Eq. (7); the magnetic moments with wave vector \mathbf{Q}_η , $m_{\mathbf{Q}_\eta}$ in Eq. (8); the number of monopoles and antimonopoles, N_m in Eq. (13); and the net scalar spin chirality χ_{sc} in Eq. (16) (note that $-\chi_{sc}$ is plotted in the figure). The green, purple, gray, and white regions represent the $4Q$ -HLs ($N_m \neq 0$), the noncoplanar $4Q$ states ($N_m = 0$), the $1Q$ conical states, and the forced ferromagnetic (FFM) state, respectively. The black-dashed vertical lines represent the topological transitions by pair annihilation of monopoles and antimonopoles, while the gray ones represent other nontopological phase transitions. The insets in (a) and (b) show the changes in the minimum distance between monopoles and antimonopoles, d_m , in Eq. (14) when increasing the field before the topological transitions. See also Figs. 5 and 6.

the biquadratic interaction, and the DM-type interaction. In other words, both spin-charge and spin-orbit couplings play a crucial role in the stabilization of the $4Q$ - and $3Q$ -HLs.

From the variational calculations, we find that the stable positions of all the monopoles and antimonopoles of the $4Q$ - and $3Q$ -HLs locate not at the lattice sites but at the interstitial positions. This is concluded for the $3Q$ -HL by the fact that the optimized phase shift in Eq. (4) always takes $\varphi_\eta = \pi/8$. In this case, the eight spins surrounding the (anti)monopole comprise a hyperbolic (anti)hedgehog the north and south poles of which are in the [111] direction, as shown in Fig. 1(c). Meanwhile, for the $4Q$ -HL, the set of φ_η depends on D and K since the four ordering vectors \mathbf{Q}_η are dependent on each other. In this case, however, the eight spins comprise a hyperbolic (anti)hedgehog with the north and south poles in the [001] direction. In both cases, the (anti)hedgehog generates an effective (anti)monopole field, as shown in Fig. 1(c). We deduce that the stable monopoles and antimonopoles centered at the interstitial positions might be ubiquitous to the systems with fixed spin length on discrete lattices since their cores are singular points where the spins vanish in the continuum limit.

V. PHASE TRANSITIONS IN MAGNETIC FIELDS

Next, we show the results for the phase diagrams of the model in Eq. (2) in the magnetic fields along the [001], [110], and [111] directions obtained by the simulated annealing in Sec. III B. In Secs. V A and V B, we present the results for the $4Q$ and $3Q$ cases, respectively.

A. $4Q$ case

Let us first discuss the $4Q$ case, the ordering vectors of which are shown in Fig. 1(a). Figure 3 summarizes the results for the $4Q$ -HL at $D = 0.3$ and $K = 0.6$.

First, we discuss the results for the [001] field, $\mathbf{h}_{001} = (0, 0, h)$, shown in Fig. 3(a). As plotted in the top panel, the magnetization m shows kinks at $h \simeq 0.575, 1.395$, and 2.335 , and a small jump at $h \simeq 0.595$. Correspondingly, the magnetic susceptibility χ shows peaks at $h \simeq 0.575$ and 0.595 , a broad hump at $h \simeq 1.395$, and a shoulder at $h \simeq 2.335$. These indicate the existence of at least four phase transitions: one at $h \simeq 0.595$ is of first order, while the remaining three are of second order. The magnetic moments $m_{\mathbf{Q}_\eta}$ plotted in the middle panel show that the four phases below $h \simeq 2.335$ are $4Q$ states with the equal amplitudes for the four $m_{\mathbf{Q}_\eta}$, whereas the phase for $h \gtrsim 2.335$ is a FFM state. We note that these $4Q$ states are distinguished by the higher Fourier components of the spin structure factor $S(\mathbf{q})$ (see Appendix A).

The number of monopoles and antimonopoles, N_m , is plotted in the bottom panel. The result shows that N_m is halved and vanishes through the second-order phase transitions at $h \simeq 0.575$ and 1.395 , respectively (black dashed lines). As plotted in the inset, the minimum distance between the monopoles and antimonopoles, d_m , gets shorter from $d_m = 2\sqrt{3}$ to 1 and 3 to 1 while approaching $h \simeq 0.575$ and 1.395 , respectively. These suggest that the phase transitions are topological ones caused by pair annihilation of monopoles and antimonopoles. We will discuss the details in Sec. VI A.

In the bottom panel, we also plot the net scalar spin chirality χ_{sc} . The result shows that χ_{sc} rapidly increases before the phase transition at $h \simeq 0.575$. After showing a sharp peak at the phase transition at $h \simeq 0.595$, χ_{sc} exhibits a broad peak at $h \sim 1$, rapidly decreases around the phase transition at $h \simeq 1.395$, and smoothly reduces to zero while approaching the phase transition to a FFM state at $h \simeq 2.335$. The change of χ_{sc} is closely related with the change in the lengths of flows of the flux Ω_p in Eq. (12); see Sec. VIA.

Next, we discuss the results for the [110] field, $\mathbf{h}_{110} = \frac{1}{\sqrt{2}}(h, h, 0)$, shown in Fig. 3(b). As shown in the top panel, m and χ show jumps and sharp peaks, respectively, at $h \simeq 0.795$, 0.845, and 1.435. m also has kinks at $h \simeq 1.325$ and 2.495, where χ shows a broad hump and a shoulder, respectively. These indicate the existence of at least five phase transitions: Three at $h \simeq 0.795$, 0.845, and 1.435 are of first order, while the remaining two at $h \simeq 1.325$ and 2.495 are of second order. $m_{\mathbf{Q}_i}$ plotted in the middle panel show that the four phases for $h \lesssim 1.435$ are $4Q$ states, the phase for $1.435 \lesssim h \lesssim 2.495$ is a single- Q ($1Q$) conical state, and that for $h \gtrsim 2.495$ is a FFM state. In the $4Q$ states, the amplitudes of $m_{\mathbf{Q}_i}$ are equal at zero field, while they split into two groups for nonzero fields. We note that the $1Q$ conical phase breaks C_2 rotational symmetry spontaneously by choosing one of two equivalent wave vectors \mathbf{Q}_3 and \mathbf{Q}_4 (we denote the chosen wave vector as \mathbf{Q}_4 in the figure).

As shown in the bottom panel of Fig. 3(b), N_m is halved through the first-order phase transition at $h \simeq 0.845$ and vanishes through the second-order one at $h \simeq 1.325$. As plotted in the inset, d_m gets shorter when approaching $h \simeq 1.325$, similar to the cases of \mathbf{h}_{001} with $h \simeq 0.575$ and 1.395. This also suggests a topological transition by pair annihilation. On the other hand, χ_{sc} has a nonzero value in all the $4Q$ states. Notably, χ_{sc} is almost doubled at $h \simeq 0.845$ where N_m is halved, and rapidly decreases through the phase transition at $h \simeq 1.325$ where N_m vanishes. We will discuss the relation to the flux flows in Sec. VIA.

Finally, we discuss the results for the [111] field, $\mathbf{h}_{111} = \frac{1}{\sqrt{3}}(h, h, h)$, shown in Fig. 3(c). m , χ , and $m_{\mathbf{Q}_i}$ in the top and middle panels signal two first-order phase transitions at $h \simeq 0.775$ and 0.845 among the $4Q$ -HLs, a first-order one to the $1Q$ conical state at $h \simeq 1.095$, and a second-order one to a FFM state at $h \simeq 2.595$. In the $4Q$ states, all four $m_{\mathbf{Q}_i}$ become inequivalent for $0.775 \lesssim h \lesssim 0.845$, while two of them have the same amplitudes for $h \lesssim 0.775$ and $0.845 \lesssim h \lesssim 1.095$. This indicates that the $4Q$ state for $0.775 \lesssim h \lesssim 0.845$ has lower symmetry compared to the other two $4Q$ states, while C_3 rotational symmetry around the [111] axis ($\parallel \mathbf{Q}_4$) is broken in all three phases except at $h = 0$.

As plotted in the bottom panel in Fig. 3(c), N_m is reduced to half through the first-order phase transition at $h \simeq 0.845$. This leads to the enhancement of χ_{sc} , similar to the case with \mathbf{h}_{110} . In the [111] field, however, the system does not exhibit a continuous phase transition that might be ascribed to the topological phase transition. This is presumably due to the fact that the $1Q$ conical state is more stable down to a lower field, compared to the [001] and [110] cases, since the field is applied in parallel to one of the wave vectors, \mathbf{Q}_4 .

B. $3Q$ case

Next, we discuss the $3Q$ case with the ordering vectors shown in Fig. 1(b). Figure 4 summarizes the results for the $3Q$ -HL at $D = 0.3$ and $K = 0.7$.

First, we discuss the results for the [001] field, $\mathbf{h}_{001} = (0, 0, h)$, shown in Fig. 4(a). As shown in the top and middle panels, m , χ , and $m_{\mathbf{Q}_i}$ signal at least five phase transitions: first-order ones at $h \simeq 0.275$, 0.695, and 0.775 and second-order ones at $h \simeq 1.035$ and 2.595. The four low-field phases for $h \lesssim 1.035$ are $3Q$ states with nonzero three $m_{\mathbf{Q}_i}$, the phase for $1.035 \lesssim h \lesssim 2.595$ is a $1Q$ conical state with only $m_{\mathbf{Q}_3} \neq 0$, and that for $h \gtrsim 2.595$ is a FFM state. Furthermore, when we look closer $m_{\mathbf{Q}_i}$, we find that $m_{\mathbf{Q}_1}$ becomes inequivalent to $m_{\mathbf{Q}_2}$ at $0.695 \lesssim h \lesssim 0.775$, whereas $m_{\mathbf{Q}_1} = m_{\mathbf{Q}_2}$ in the other three $3Q$ states. These $3Q$ states are also distinguished by the higher Fourier components of the spin structure factor $S(\mathbf{q})$ and the structure factor of the local scalar spin chirality (see Appendix B).

As shown in the bottom panel of Fig. 4(a), N_m is unchanged in the three low-field $3Q$ phases, but it vanishes through the first-order phase transition at $h \simeq 0.775$. On the other hand, χ_{sc} increases in the two low-field phases, while it rapidly decreases in the third phase and vanishes through the second-order phase transition to the $1Q$ conical state at $h \simeq 1.035$. The change of χ_{sc} in the $3Q$ -HL phases is accounted for by the change in the lengths of the flux flows connecting the monopoles and antimonopoles, similar to the $4Q$ case in Sec. VA (see Sec. VIB).

Next, we discuss the results for the [110] field, $\mathbf{h}_{110} = \frac{1}{\sqrt{2}}(h, h, 0)$, shown in Fig. 4(b). As plotted in the top panel, the data of m and χ signal seven first-order phase transitions at $h \simeq 0.405$, 0.525, 0.725, 0.975, 0.995, 1.125, and 1.245, and a second-order phase transition at $h \simeq 2.415$. In addition, $m_{\mathbf{Q}_i}$ in the middle panel and N_m in the bottom panel indicate additional phase transitions at $h \simeq 0.445$, 0.745, 0.945, and 1.355. $m_{\mathbf{Q}_i}$ shows that all the phases for $h \lesssim 1.245$ are $3Q$ states, the two phases for $1.245 \lesssim h \lesssim 2.415$ are $2Q$ states, and the phase for $h \gtrsim 2.415$ is a FFM state. We note that $m_{\mathbf{Q}_1}$ becomes inequivalent to $m_{\mathbf{Q}_2}$ in the $3Q$ states for $0.405 \lesssim h \lesssim 0.525$ and $0.725 \lesssim h \lesssim 0.975$, and the $2Q$ state for $1.245 \lesssim h \lesssim 1.355$. This indicates spontaneous symmetry breaking by choosing one of the two equivalent wave vectors in these states.

Within the $3Q$ phases for $h \lesssim 1.245$, N_m changes in a complicated manner, as plotted in the bottom panel of Fig. 4(b): In contrast to the other cases, N_m is not reduced monotonically but changes from 8 to 6 to 10 to 6 to 2 in steps. By tracing d_m plotted in the insets, we find that the three phase transitions at $h \simeq 0.445$, 0.745, and 0.945 appear to be topological ones caused by pair annihilation of monopoles and antimonopoles (d_m does not change from 1 before the transitions since the lattice spacing is larger than the positional changes of monopoles and antimonopoles; see Sec. VIB for the details). The net scalar spin chirality χ_{sc} is nonzero in all the $3Q$ -HLs for $0 < h \lesssim 1.245$. It exhibits a broad peak at $h \sim 1$ and vanishes through the first-order phase transition to the $2Q$ state at $h \simeq 1.245$.

Finally, we discuss the results for the [111] field, $\mathbf{h}_{111} = \frac{1}{\sqrt{3}}(h, h, h)$, shown in Fig. 4(c). In this case, m and χ plotted

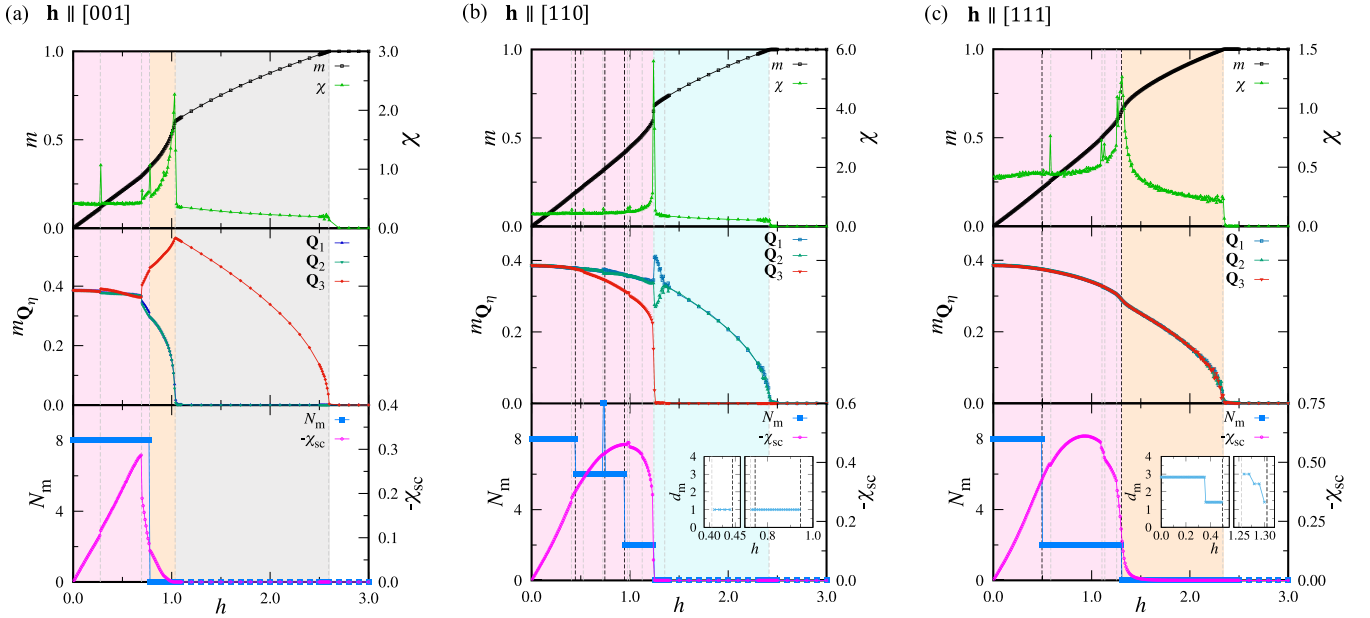


FIG. 4. Phase transitions in the magnetic field along the (a) [001], (b) [110], and (c) [111] directions in the 3Q case. The plotted quantities and the dashed vertical lines for the phase transitions are common to those in Fig. 3. The red, orange, blue, gray, and white regions represent the 3Q-HLs ($N_m \neq 0$), the noncoplanar 3Q states ($N_m = 0$), the 2Q vortex crystal states, the 1Q conical state, and the FFM state, respectively. See also Figs. 7 and 8 for the changes of d_m shown in the insets of the bottom panels of (b) and (c).

in the top panel signal four first-order phase transitions at $h \simeq 0.585, 1.105, 1.135,$ and 1.255 , and two second-order ones at $h \simeq 1.305$ and 2.335 . In addition, N_m in the bottom panel indicates an additional phase transition at $h \simeq 0.495$. m_{Q_i} in the middle panel shows that all the phases for $h \lesssim 2.335$ are 3Q states, while the phase for $h \gtrsim 2.335$ is a FFM state. All the 3Q phases have the equal amplitudes for the three m_{Q_i} ; namely, they retain C_3 rotational symmetry with respect to the [111] axis.

As plotted in the bottom panel of Fig. 4(c), N_m is nonzero in the 3Q phases below $h \simeq 1.305$. By monitoring d_m plotted in the insets, we find that the transitions at $h \simeq 0.495$ and 1.305 appear to be topological ones by pair annihilation of monopoles and antimonopoles. χ_{sc} is nonzero for all the 3Q-HLs but decreases rapidly through the second-order phase transition at $h \simeq 1.305$ where N_m vanishes. We will discuss the details in Sec. VI B.

VI. TOPOLOGICAL PHASE TRANSITIONS BY PAIR ANNIHILATION OF MONOPOLES AND ANTIMONOPOLES

In Sec. V, we found several phase transitions in the 4Q- and 3Q-HL phases where no discontinuous changes are observed in m and m_{Q_i} but N_m changes. These suggest continuous phase transitions with a topological change caused by pair annihilation of monopoles and antimonopoles. Such topological transitions under the [001] field were discussed for an ansatz of the 3Q-HL state in the continuum limit [10] and also for a metastable 3Q-HL in the model in Eq. (2) [40]. Our results in Sec. V, however, appear to offer several examples in the ground state for both 4Q- and 3Q-HLs. In this section, we analyze these phase transitions by tracing the positions of monopoles and antimonopoles in real space. In Secs. VI A

and VI B, we present the results for the 4Q and 3Q cases, respectively.

A. 4Q case

In Sec. V A, we found three possible topological phase transitions in the 4Q-HL: Two are at $h \simeq 0.575$ and 1.395 for the [001] field and the other is at $h \simeq 1.325$ for the [110] field. We discuss how the monopoles and antimonopoles move and pair annihilate as a function of the field strength through each transition.

In the case of the [001] field, N_m changes from 16 to 8 at $h \simeq 0.575$ and from 8 to 0 at $h \simeq 1.395$, both suggesting four pairs of monopoles and antimonopoles annihilate simultaneously at the phase transition. They are visualized in real space in Fig. 5. At zero field, the monopoles and antimonopoles form two interpenetrating body-centered-cubic lattices with $d_m = 2\sqrt{3}$ as shown in Fig. 5(a) [see also Fig. 1(a)]. While increasing h , half of the monopoles and antimonopoles move toward each other in the field direction, forming four pairs. When approaching to the critical field, d_m given by the four pairs is reduced to 1 as shown in Fig. 5(b) at $h = 0.57$ and then becomes zero, which is the pair annihilation at the critical field $h \simeq 0.575$. In the higher-field region, the remaining monopoles and antimonopoles are paired along the field direction again, as exemplified in Fig. 5(c) at $h = 0.60$. In this case, d_m is reduced from 3 to 1 as shown in Fig. 5(d) at $h = 1.39$ and, finally, becomes zero at the critical field $h \simeq 1.395$ by the pair annihilation. The changes of d_m were plotted in the inset of the bottom panel in Fig. 3(a).

The movement of the monopoles and antimonopoles explains the behavior of χ_{sc} plotted in the bottom panel of Fig. 3(a). When approaching the topological transition at

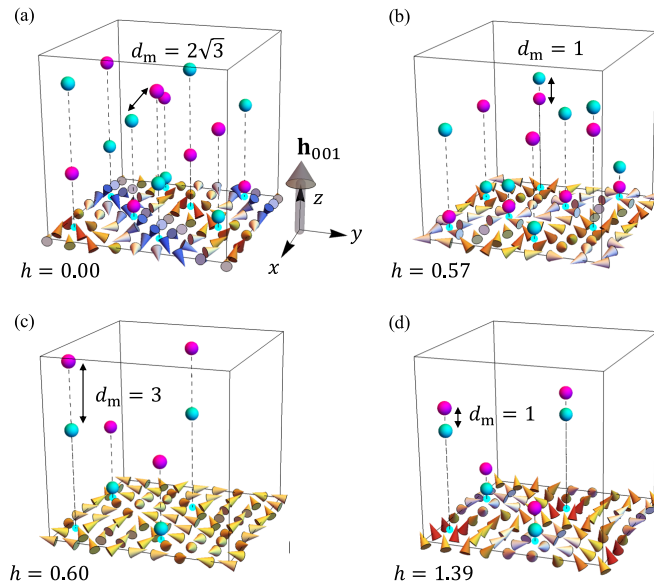


FIG. 5. Positions of monopoles (magenta) and antimonopoles (cyan) in the magnetic unit cell (cube) when approaching the topological transition at $h \simeq 0.575$ and 1.395 for the $[001]$ field (denoted by the gray arrow) in the $4Q$ case: (a) $h = 0.00$, (b) $h = 0.57$, (c) $h = 0.60$, and (d) $h = 1.39$. The arrows at the bottom show the slice of the spin texture on the plane just below some of the monopoles and antimonopoles. The black arrows represent the minimum distances between the monopoles and antimonopoles, d_m . The vertical dashed lines and the dots at the bottom end represent the projections onto the bottom plane as guides for the eye.

$h \simeq 0.575$ by increasing h , χ_{sc} decreases [$-\chi_{sc}$ increases in Fig. 3(a)]. This is understood by the decrease of d_m with the flux flows in the same direction of the magnetic field: The decrease of d_m reduces the positive contribution to χ_{sc} , which leads to the net decrease in χ_{sc} . On the other hand, χ_{sc} increases ($-\chi_{sc}$ decreases) near the other topological transition at $h \simeq 1.395$. This is due to the decrease of d_m with the flux flows in the opposite direction to the magnetic field.

Similarly, N_m changes from 8 to 0 for the $[110]$ field through the phase transition at $h \simeq 1.325$. The change of the positions of monopoles and antimonopoles is shown in Fig. 6, where d_m changes in a similar manner to the case of the $[001]$ field at $h \simeq 1.395$ in Figs. 5(c) and 5(d); see also the inset of

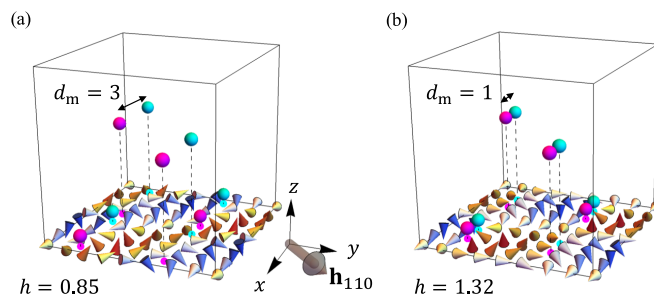


FIG. 6. Positions of monopoles and antimonopoles when approaching the topological transition at $h \simeq 1.325$ for the $[110]$ field in the $4Q$ case: (a) $h = 0.85$ and (b) $h = 1.32$. The notations are common to those in Fig. 5.

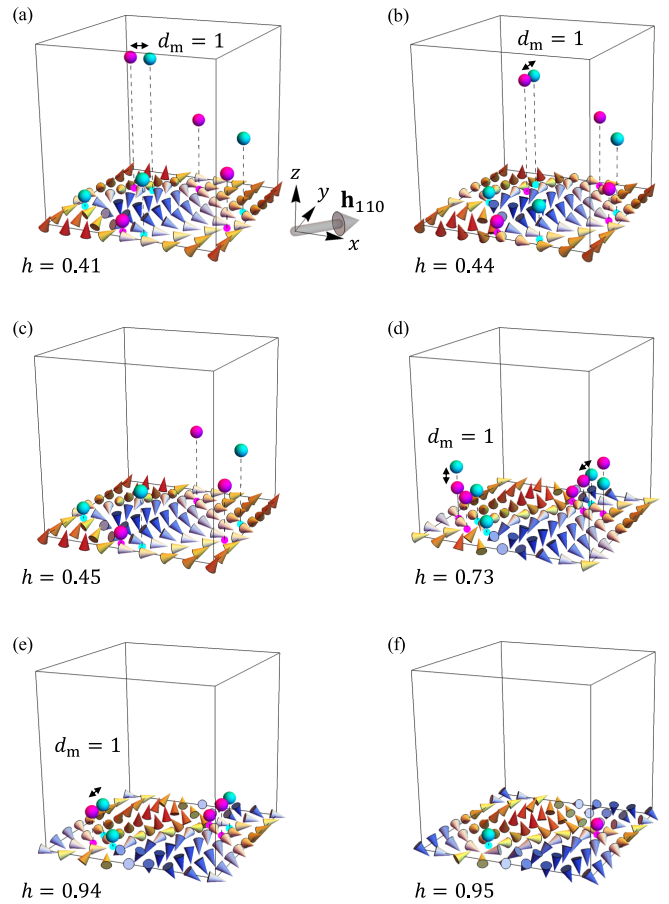


FIG. 7. Positions of monopoles and antimonopoles when approaching the topological transition at $h \simeq 0.445$, 0.745 , and 0.945 for the $[110]$ field in the $3Q$ case: (a) $h = 0.41$, (b) $h = 0.44$, (c) $h = 0.45$, (d) $h = 0.73$, (e) $h = 0.94$, and (f) $h = 0.95$. The notations are common to those in Fig. 5.

the bottom panel of Fig. 3(b). The only difference from the $[001]$ case is in the direction of collisions. The corresponding reduction of the lengths of the flux flows is also related to the suppression of χ_{sc} in Fig. 3(b) since the fluxes Ω_p have the positive component in the opposite direction to the field.

B. $3Q$ case

In the case of the $3Q$ -HLs, we identified totally five possible topological transitions in Sec. VB. Three of them are at $h \simeq 0.445$, 0.745 , and 0.945 for the $[110]$ field, and the remaining two are at $h \simeq 0.495$ and 1.305 for the $[111]$ field. Figure 7 shows the real-space pictures for the $[110]$ field. In a low field, there are totally eight monopoles and antimonopoles as shown in Fig. 7(a) for $h = 0.41$, but one pair annihilates through the transition at $h \simeq 0.445$ as shown in Figs. 7(b) and 7(c). We note that the directions of pairs change within the same $3Q$ state with spontaneous symmetry breaking with respect to the $[100]$ and $[010]$ directions. In the next topological transition at $h \simeq 0.745$, N_m changes from 10 to 6, where two pairs of monopoles and antimonopoles annihilate as shown in Figs. 7(d) and 7(e). Through these transitions, d_m does not change from 1, since the distance for the pairs that survive is already 1 before the transition.

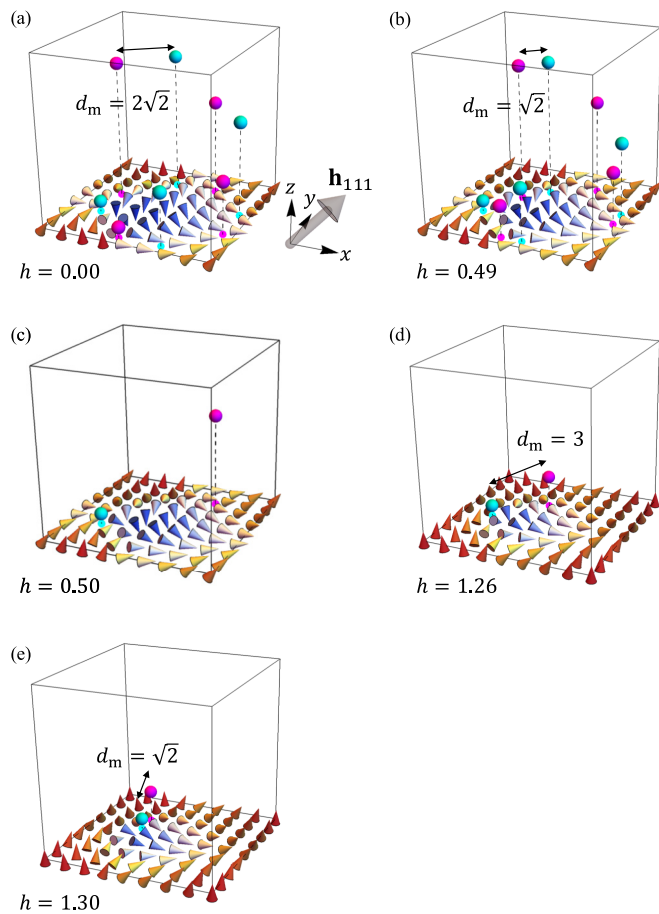


FIG. 8. Positions of monopoles and antimonopoles when approaching the topological transition at $h \simeq 0.495$ and 1.305 for the $[111]$ field in the $3Q$ case: (a) $h = 0.00$, (b) $h = 0.49$, (c) $h = 0.50$, (d) $h = 1.26$, and (e) $h = 1.30$. The notations are common to those in Fig. 5.

Finally, the other two pairs annihilate and N_m is reduced to 2 at $h \simeq 0.945$ as shown in Fig. 7(f). See also the insets in the bottom panel of Fig. 4(b).

Finally, we present the results for the $[111]$ field in Fig. 8. In this case, there are four pairs of monopoles and antimonopoles in the low-field phase, and their distance gets shorter as demonstrated in Figs. 8(a) and 8(b). Through the topological transition at $h \simeq 0.495$, three of four annihilate as shown in Fig. 8(c). Finally, the remaining pair gets closer and pair annihilates through the transition at $h \simeq 1.305$ as shown in Figs. 8(d) and 8(e). The rapid decrease of d_m explains the rapid suppression of χ_{sc} while approaching the topological phase transition at $h \simeq 1.305$ in Fig. 4(c).

VII. CONCLUDING REMARKS

In conclusion, we have investigated the magnetic HLs in the effective spin model with long-range interactions reflecting the itinerant nature of electrons. We found that both $4Q$ - and $3Q$ -HLs are stabilized even at zero magnetic field by the synergy between the DM-type interactions from the spin-orbit coupling and the multiple-spin interactions from the spin-charge coupling. The results are in stark contrast

to the previous studies for the localized spin models with short-range interactions, where the HLs are stable only in a field. Furthermore, our HLs may have much shorter periods compared to the previous ones; the periods in our HLs are dictated by nesting properties of the Fermi surface, whereas those in the previous studies are given by the competition between the ferromagnetic exchange interaction and the DM interaction. We also clarified the effect of an external magnetic field on the HLs. We showed that both $4Q$ and $3Q$ cases exhibit a variety of successive phase transitions depending on the field direction, including the transitions to $2Q$ and $1Q$ states. Interestingly, among them, we found several topological phase transitions where the number of monopoles and antimonopoles changes by the pair annihilation. We explicitly showed how the pair annihilation occurs by tracing the real-space positions of monopoles and antimonopoles on the discrete lattice.

As mentioned in the introduction, $3Q$ - and $4Q$ -HLs were recently discovered in $\text{MnSi}_{1-x}\text{Ge}_x$ [6,7,14]. They are stable even in the absence of the magnetic field and have much shorter periods compared to the conventional skyrmion lattices, for instance, in MnSi , and evaded the understanding from the conventional spin models with short-range two-spin interactions. A scenario was recently proposed based on short-range four-spin and six-spin interactions including the scalar spin chirality [23]. Our finding suggests another scenario by emphasizing the important role of the itinerant nature of electrons. To test our scenario, it is necessary to clarify the electronic structure in the real compounds, e.g., by the angle-resolved photoemission spectroscopy and the de Haas–van Alphen effect. First-principles calculations would also be helpful, while it is not straightforward to precisely predict the relevant wave numbers in the complicated multiorbital systems with electron correlations, in particular, chemically doped materials like $\text{MnSi}_{1-x}\text{Ge}_x$. It would also be interesting to test our scenario for the short-period skyrmion lattice recently discovered in EuPtSi [42–44]. We note that a similar scenario (without the DM-type interaction) was recently discussed for the swirling spin textures in a centrosymmetric triangular magnet Gd_2PdSi_3 [45].

On the other hand, in the magnetic field, our results suggest that the $4Q$ and $3Q$ states exhibit a nonzero topological Hall effect through the nonzero scalar spin chirality χ_{sc} . Our results also indicate that χ_{sc} changes drastically corresponding to the modulation of the magnetic textures including the topological transitions by pair annihilations of monopoles and antimonopoles. Experimentally, interesting behaviors were observed in a wide range of field and temperature, even with the sign change of the topological Hall resistivity [14]. Assuming our scenario based on the itinerant nature of electrons, it will be important to take into account the realistic electronic band structures in the magnetic field for detailed comparison between theory and experiment. In particular, it is worth studying how the modulations of the Fermi surfaces and corresponding \mathbf{Q}_η modify the phase diagrams in the magnetic field. Moreover, thermal fluctuations might also play an important role. We leave the finite-temperature study as a future work, as it requires sophisticated Monte Carlo simulations beyond the simulated annealing to resolve competing phases.

ACKNOWLEDGMENTS

We would like to thank N. Kanazawa and K. Shimizu for fruitful discussions. This research was supported by Grants-in-Aid for Scientific Research under Grants No. JP19H05825 and No. JP18K13488; JST CREST (Grant No. JP-MJCR18T2); the Chirality Research Center in Hiroshima University; and the Japan Society for the Promotion of Science (JSPS) Core-to-Core Program, Advanced Research Networks. S.O. was supported by JSPS through a research fellowship for young scientists.

APPENDIX A: DIFFERENCE AMONG THE $4Q$ STATES

In this section, we discuss the difference among the $4Q$ states found in Sec. V A. In the case of the [001] field in Fig. 3(a), we found four $4Q$ states below $h \simeq 2.335$, all of which have the equal amplitudes of the four $m_{\mathbf{Q}_\eta}$. Two of them are distinguished by the number of monopoles and antimonopoles, N_m : the $4Q$ -HL state with $N_m = 16$ below $h \simeq 0.575$ and the $4Q$ state with $N_m = 0$ above $h \simeq 1.395$. The remaining two have the same $N_m = 8$, but we find that they show different values in higher harmonics in the spin structure factor $S(\mathbf{q})$ in Eq. (9): By calculating $S(\mathbf{Q}_\eta + \mathbf{Q}_{\eta'})$ where $\eta = 1, 2, 3, 4$ and $\eta \neq \eta'$, we find that $S(\mathbf{Q}_2 + \mathbf{Q}_3)$ and $S(\mathbf{Q}_3 + \mathbf{Q}_1)$ have equal amplitudes for $0.575 \lesssim h \lesssim 0.595$, but $S(\mathbf{Q}_2 + \mathbf{Q}_3) \neq S(\mathbf{Q}_3 + \mathbf{Q}_1)$ for $0.595 \lesssim h \lesssim 1.395$. The differences among the four $4Q$ states are summarized in Fig. 9(a).

In the case of the [110] field in Fig. 3(b), we also find four $4Q$ states below $h \simeq 1.435$ that share the same symmetry in terms of $m_{\mathbf{Q}_\eta}$. In this case again, N_m distinguishes two of them: the $4Q$ -HL state with $N_m = 8$ for $0.845 \lesssim h \lesssim 1.325$ and the $4Q$ state with $N_m = 0$ for $1.325 \lesssim h \lesssim 1.435$. In order to distinguish the remaining two for $h \lesssim 0.845$, we calculate the spin structure factor with the spin component parallel to the [110] field defined by

$$S^{\parallel}(\mathbf{q}) = \frac{1}{2} \{ S^{\text{xx}}(\mathbf{q}) + S^{\text{yy}}(\mathbf{q}) \} + S^{\text{xy}}(\mathbf{q}), \quad (\text{A1})$$

where $S^{\mu\nu}(\mathbf{q})$ is the matrix form of the spin structure factor defined by

$$S^{\mu\nu}(\mathbf{q}) = \frac{1}{N} \sum_{l,l'} S_{\mathbf{r}_l}^{\mu} S_{\mathbf{r}_{l'}}^{\nu} e^{-i\mathbf{q}\cdot(\mathbf{r}_l - \mathbf{r}_{l'})}. \quad (\text{A2})$$

We find that the higher harmonics along the field direction, $S^{\parallel}(2\mathbf{Q}_1 + 2\mathbf{Q}_2)$, is nonzero in the $4Q$ state for $0.795 \lesssim h \lesssim 0.845$, while it vanishes for $h \lesssim 0.795$. The differences among the four $4Q$ states are summarized in Fig. 9(b).

Finally, in the case of the [111] field in Fig. 3(c), we find three $4Q$ states. In this case, $m_{\mathbf{Q}_\eta}$ distinguishes the intermediate phase for $0.845 \lesssim h \lesssim 1.095$, as mentioned in Sec. V A. The remaining two can be distinguished by N_m . See Fig. 9(c).

APPENDIX B: DIFFERENCE AMONG THE $3Q$ STATES

In this section, we discuss the difference among the $3Q$ states found in Sec. V B. In the case of the [001] field in Fig. 4(a), we find four $3Q$ states. One of them for $0.775 \lesssim$

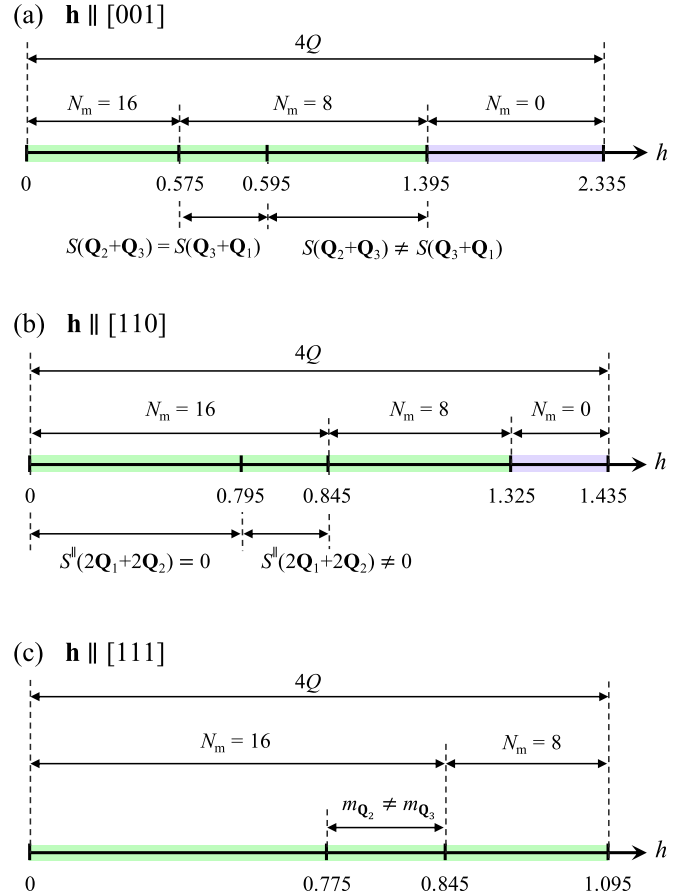


FIG. 9. Schematics for the differences among the $4Q$ phases in the (a) [001], (b) [110], and (c) [111] field corresponding to Figs. 3(a), 3(b), and 3(c), respectively.

$h \lesssim 1.035$ is distinguished from the others by N_m : the $3Q$ state with $N_m = 0$ above $h \simeq 0.775$. In addition, as mentioned in Sec. V B, $m_{\mathbf{Q}_\eta}$ distinguishes the $3Q$ -HL state for $0.695 \lesssim h \lesssim 0.775$. We find a difference between the remaining two in higher harmonics in the structure factor of the local scalar spin chirality in Eq. (15). Specifically, we calculate the component perpendicular to the [001] field defined by

$$\chi_{\text{sc}}^{\perp}(\mathbf{q}) = \frac{1}{2} \{ \chi_{\text{sc}}^{\text{xx}}(\mathbf{q}) + \chi_{\text{sc}}^{\text{yy}}(\mathbf{q}) \} + \chi_{\text{sc}}^{\text{xy}}(\mathbf{q}), \quad (\text{B1})$$

where $\chi_{\text{sc}}^{\mu\nu}(\mathbf{q})$ is the matrix form of the structure factor defined by

$$\chi_{\text{sc}}^{\mu\nu}(\mathbf{q}) = \frac{1}{N} \sum_{l,l'} \chi_{\text{sc}}^{\mu}(\mathbf{r}_l) \chi_{\text{sc}}^{\nu}(\mathbf{r}_{l'}) e^{-i\mathbf{q}\cdot(\mathbf{r}_l - \mathbf{r}_{l'})}. \quad (\text{B2})$$

We find that $\chi_{\text{sc}}^{\perp}(2\mathbf{Q}_1)$ and $\chi_{\text{sc}}^{\perp}(2\mathbf{Q}_2)$ are nonzero and have equal amplitudes in the $3Q$ -HL state for $0.275 \lesssim h \lesssim 0.695$, but vanish below $h \simeq 0.275$. The differences among the four $3Q$ states are summarized in Fig. 10(a).

Next, in the case of the [110] field in Fig. 4(b), we found ten $3Q$ states below $h \simeq 1.245$ with a variety of N_m . The $3Q$ -HL state with $N_m = 10$ for $0.725 \lesssim h \lesssim 0.745$ is distinguished from others, but $N_m = 8$ for the two states below $h \simeq 0.445$, $N_m = 6$ for the three states for $0.445 \lesssim h \lesssim 0.725$

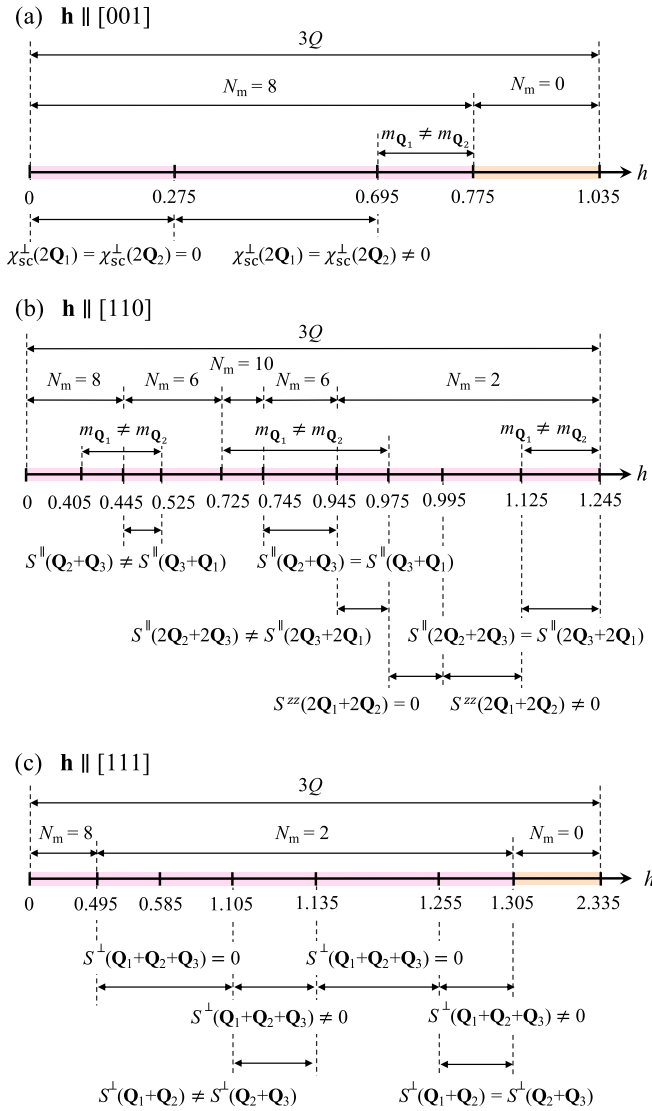


FIG. 10. Schematics of the $3Q$ states in the (a) [001], (b) [110], and (c) [111] field corresponding to Figs. 4(a), 4(b), and 4(c), respectively.

and $0.745 \lesssim h \lesssim 0.945$, and $N_m = 2$ for the remaining four for $0.945 \lesssim h \lesssim 1.245$. As mentioned in Sec. VB, the two with $N_m = 8$ below $h \simeq 0.445$ and the two with $N_m = 6$ for $0.445 \lesssim h \lesssim 0.725$ are distinguished by $m_{\mathbf{Q}_\eta}$. Similarly, the two with $N_m = 2$ for $0.945 \lesssim h \lesssim 0.975$ and $1.125 \lesssim h \lesssim 1.245$ are distinguished from the other two by $m_{\mathbf{Q}_\eta}$. See Fig. 10(b).

In order to distinguish the rest, we calculate higher harmonics in the spin structure factor similar to the $4Q$ case in Appendix A. For the $3Q$ -HL states with $N_m = 6$, $S^\parallel(\mathbf{Q}_2 + \mathbf{Q}_3)$ and $S^\parallel(\mathbf{Q}_3 + \mathbf{Q}_1)$ have equal amplitudes for $0.745 \lesssim h \lesssim 0.945$, but do not for $0.445 \lesssim h \lesssim 0.525$. Meanwhile, for the two states with $N_m = 2$ and $m_{\mathbf{Q}_1} \neq m_{\mathbf{Q}_2}$, $S^\parallel(2\mathbf{Q}_2 + 2\mathbf{Q}_3) = S^\parallel(2\mathbf{Q}_3 + 2\mathbf{Q}_1)$ for $1.125 \lesssim h \lesssim 1.245$ while $S^\parallel(2\mathbf{Q}_2 + 2\mathbf{Q}_3) \neq S^\parallel(2\mathbf{Q}_3 + 2\mathbf{Q}_1)$ for $0.945 \lesssim h \lesssim 0.975$. Furthermore, for the two states with $N_m = 2$ and $m_{\mathbf{Q}_1} = m_{\mathbf{Q}_2}$ the component perpendicular to the [110] field, $S^{zz}(2\mathbf{Q}_1 + 2\mathbf{Q}_2)$, is zero for $0.975 \lesssim h \lesssim 0.995$, but nonzero for $0.995 \lesssim h \lesssim 1.125$. All the differences among the ten $3Q$ states are summarized in Fig. 10(b).

Finally, in the case of the [111] field in Fig. 4(c), we found seven $3Q$ states below $h \simeq 2.335$, all of which have equal amplitudes of the three $m_{\mathbf{Q}_\eta}$. Two of them are distinguished by N_m : the $3Q$ -HL state with $N_m = 8$ below $h \simeq 0.495$ and the $3Q$ state with $N_m = 0$ above $h \simeq 1.305$. The remaining five have the same $N_m = 2$, but two of them for $1.105 \lesssim h \lesssim 1.135$ and $1.255 \lesssim h \lesssim 1.305$ show nonzero values in higher harmonics in the spin structure factor $S^\perp(\mathbf{Q}_1 + \mathbf{Q}_2 + \mathbf{Q}_3)$, which is the component perpendicular to the [111] field given by

$$S^\perp(\mathbf{q}) = \frac{2}{3} \{S(\mathbf{q}) - S^{xy}(\mathbf{q}) - S^{yz}(\mathbf{q}) - S^{zx}(\mathbf{q})\}. \quad (\text{B3})$$

Furthermore, $S^\perp(\mathbf{Q}_1 + \mathbf{Q}_2) = S^\perp(\mathbf{Q}_2 + \mathbf{Q}_3)$ for $1.105 \lesssim h \lesssim 1.135$, but $S^\perp(\mathbf{Q}_1 + \mathbf{Q}_2) \neq S^\perp(\mathbf{Q}_2 + \mathbf{Q}_3)$ for $1.255 \lesssim h \lesssim 1.305$. The remaining three $3Q$ -HLs (for $0.495 \lesssim h \lesssim 0.585$, $0.585 \lesssim h \lesssim 1.105$, and $1.135 \lesssim h \lesssim 1.255$) with $N_m = 2$ cannot be distinguished within the present analyses although further higher harmonics may reveal the difference. See Fig. 10(c).

- [1] N. Nagaosa and Y. Tokura, Topological properties and dynamics of magnetic skyrmions, *Nat. Nano.* **8**, 899 (2013).
- [2] Y. Togawa, Y. Kousaka, K. Inoue, and J. Kishine, Symmetry, Structure, and Dynamics of Monoaxial Chiral Magnets, *J. Phys. Soc. Jpn.* **85**, 112001 (2016).
- [3] Y. Tokura and S. Seki, Multiferroics with Spiral Spin Orders, *Adv. Mater.* **22**, 1554 (2010).
- [4] M. Mochizuki and S. Seki, Dynamical magnetoelectric phenomena of multiferroic skyrmions, *J. Phys.: Condens. Matter* **27**, 503001 (2015).
- [5] Y. Tokura and N. Nagaosa, Nonreciprocal responses from noncentrosymmetric quantum materials, *Nat. Commun.* **9**, 3740 (2018).
- [6] T. Tanigaki, K. Shibata, N. Kanazawa, X. Yu, Y. Onose, H. S. Park, D. Shindo, and Y. Tokura, Real-space observation of

short-period cubic lattice of skyrmions in MnGe, *Nano Lett.* **15**, 5438 (2015).

- [7] N. Kanazawa, S. Seki, and Y. Tokura, Noncentrosymmetric magnets hosting magnetic skyrmions, *Adv. Mater.* **29**, 1603227 (2017).
- [8] N. Kanazawa, J.-H. Kim, D. S. Inosov, J. S. White, N. Egetenmeyer, J. L. Gavilano, S. Ishiwata, Y. Onose, T. Arima, B. Keimer, and Y. Tokura, Possible skyrmion-lattice ground state in the $B20$ chiral-lattice magnet MnGe as seen via small-angle neutron scattering, *Phys. Rev. B* **86**, 134425 (2012).
- [9] N. Kanazawa, Y. Nii, X. X. Zhang, A. S. Mishchenko, G. D. Filippis, F. Kagawa, Y. Iwasa, N. Nagaosa, and Y. Tokura, Critical phenomena of emergent magnetic monopoles in a chiral magnet, *Nat. Commun.* **7**, 11622 (2016).

- [10] X.-X. Zhang, A. S. Mishchenko, G. De Filippis, and N. Nagaosa, Electric transport in three-dimensional skyrmion/monopole crystal, *Phys. Rev. B* **94**, 174428 (2016).
- [11] N. Kanazawa, Y. Onose, T. Arima, D. Okuyama, K. Ohoyama, S. Wakimoto, K. Kakurai, S. Ishiwata, and Y. Tokura, Large Topological Hall Effect in a Short-Period Helimagnet MnGe, *Phys. Rev. Lett.* **106**, 156603 (2011).
- [12] Y. Shiomi, N. Kanazawa, K. Shibata, Y. Onose, and Y. Tokura, Topological Nernst effect in a three-dimensional skyrmion-lattice phase, *Phys. Rev. B* **88**, 064409 (2013).
- [13] Y. Fujishiro, N. Kanazawa, T. Shimojima, A. Nakamura, K. Ishizaka, T. Koretsune, R. Arita, A. Miyake, H. Mitamura, K. Akiba, M. Tokunaga, J. Shiogai, S. Kimura, S. Awaji, A. Tsukazaki, A. Kikkawa, Y. Taguchi, and Y. Tokura, Large magneto-thermopower in MnGe with topological spin texture, *Nat. Commun.* **9**, 408 (2018).
- [14] Y. Fujishiro, N. Kanazawa, T. Nakajima, X. Z. Yu, K. Ohishi, Y. Kawamura, K. Kakurai, T. Arima, H. Mitamura, A. Miyake, K. Akiba, M. Tokunaga, A. Matsuo, K. Kindo, T. Koretsune, R. Arita, and Y. Tokura, Topological transitions among skyrmion- and hedgehog-lattice states in cubic chiral magnets, *Nat. Commun.* **10**, 1059 (2019).
- [15] B. Binz and A. Vishwanath, Theory of helical spin crystals: Phases, textures, and properties, *Phys. Rev. B* **74**, 214408 (2006).
- [16] J.-H. Park and J. H. Han, Zero-temperature phases for chiral magnets in three dimensions, *Phys. Rev. B* **83**, 184406 (2011).
- [17] S.-G. Yang, Y.-H. Liu, and J. H. Han, Formation of a topological monopole lattice and its dynamics in three-dimensional chiral magnets, *Phys. Rev. B* **94**, 054420 (2016).
- [18] I. Dzyaloshinsky, A thermodynamic theory of “weak” ferromagnetism of antiferromagnetics, *J. Phys. Chem. Solids* **4**, 241 (1958).
- [19] T. Moriya, Anisotropic superexchange interaction and weak ferromagnetism, *Phys. Rev.* **120**, 91 (1960).
- [20] J. Gayles, F. Freimuth, T. Schena, G. Lani, P. Mavropoulos, R. A. Duine, S. Blügel, J. Sinova, and Y. Mokrousov, Dzyaloshinskii-Moriya Interaction and Hall Effects in the Skyrmion Phase of $\text{Mn}_{1-x}\text{Fe}_x\text{Ge}$, *Phys. Rev. Lett.* **115**, 036602 (2015).
- [21] T. Koretsune, N. Nagaosa, and R. Arita, Control of Dzyaloshinskii-Moriya interaction in $\text{Mn}_{1-x}\text{Fe}_x\text{Ge}$: A first-principles study, *Sci. Rep.* **5**, 13302 (2015).
- [22] T. Kikuchi, T. Koretsune, R. Arita, and G. Tatara, Dzyaloshinskii-Moriya Interaction as a Consequence of a Doppler Shift due to Spin-Orbit-Induced Intrinsic Spin Current, *Phys. Rev. Lett.* **116**, 247201 (2016).
- [23] S. Grytsiuk, M. Hoffmann, J.-P. Hanke, P. Mavropoulos, Y. Mokrousov, G. Bihlmayer, and S. Blügel, *Ab initio* analysis of magnetic properties of the prototype B20 chiral magnet FeGe, *Phys. Rev. B* **100**, 214406 (2019).
- [24] S. Brinker, M. d. S. Dias, and S. Lounis, The chiral biquadratic pair interaction, *New J. Phys.* **21**, 083015 (2019).
- [25] S. Grytsiuk, J.-P. Hanke, M. Hoffmann, J. Bouaziz, O. Gomonay, G. Bihlmayer, Y. Mokrousov, and S. Blügel, Topological chiral magnetic interactions driven by emergent orbital magnetism, *Nat. Commun.* **11**, 511 (2020).
- [26] G. R. Stewart, Heavy-fermion systems, *Rev. Mod. Phys.* **56**, 755 (1984).
- [27] P. Gegenwart, Q. Si, and F. Steglich, Quantum criticality in heavy-fermion metals, *Nat. Phys.* **4**, 186 (2008).
- [28] I. Martin and C. D. Batista, Itinerant Electron-Driven Chiral Magnetic Ordering and Spontaneous Quantum Hall Effect in Triangular Lattice Models, *Phys. Rev. Lett.* **101**, 156402 (2008).
- [29] C. Zener, Interaction between the d -shells in the transition metals. II. ferromagnetic compounds of manganese with perovskite structure, *Phys. Rev.* **82**, 403 (1951).
- [30] P. W. Anderson and H. Hasegawa, Considerations on double exchange, *Phys. Rev.* **100**, 675 (1955).
- [31] M. A. Ruderman and C. Kittel, Indirect exchange coupling of nuclear magnetic moments by conduction electrons, *Phys. Rev.* **96**, 99 (1954).
- [32] T. Kasuya, A theory of metallic ferro- and antiferromagnetism on Zener’s model, *Prog. Theor. Phys.* **16**, 45 (1956).
- [33] K. Yosida, Magnetic properties of Cu-Mn alloys, *Phys. Rev.* **106**, 893 (1957).
- [34] Y. Akagi, M. Udagawa, and Y. Motome, Hidden Multiple-Spin Interactions as an Origin of Spin Scalar Chiral Order in Frustrated Kondo Lattice Models, *Phys. Rev. Lett.* **108**, 096401 (2012).
- [35] S. Hayami and Y. Motome, Multiple- Q instability by $(d - 2)$ -dimensional connections of Fermi surfaces, *Phys. Rev. B* **90**, 060402(R) (2014).
- [36] S. Hayami, R. Ozawa, and Y. Motome, Effective bilinear-biquadratic model for noncoplanar ordering in itinerant magnets, *Phys. Rev. B* **95**, 224424 (2017).
- [37] S. Hayami and Y. Motome, Néel- and Bloch-Type Magnetic Vortices in Rashba Metals, *Phys. Rev. Lett.* **121**, 137202 (2018).
- [38] The perturbation expansion for Eq. (1) leads to $\mathbf{D}_\eta \parallel \mathbf{Q}_\eta$ [37].
- [39] R. Ozawa, S. Hayami, K. Barros, G.-W. Chern, Y. Motome, and C. D. Batista, Vortex Crystals with Chiral Stripes in Itinerant Magnets, *J. Phys. Soc. Jpn.* **85**, 103703 (2016).
- [40] S. Okumura, S. Hayami, Y. Kato, and Y. Motome, Tracing monopoles and anti-monopoles in a magnetic hedgehog lattice, *JPS Conf. Proc.* **30**, 011010 (2020).
- [41] B. Binz and A. Vishwanath, Chirality induced anomalous-Hall effect in helical spin crystals, *Physica B* **403**, 1336 (2008).
- [42] M. Kakihana, D. Aoki, A. Nakamura, F. Honda, M. Nakashima, Y. Amako, S. Nakamura, T. Sakakibara, M. Hedo, T. Nakama, and Y. Nuki, Giant hall resistivity and magnetoresistance in cubic chiral antiferromagnet EuPtSi, *J. Phys. Soc. Jpn.* **87**, 023701 (2018).
- [43] K. Kaneko, M. D. Frontzek, M. Matsuda, A. Nakao, K. Munakata, T. Ohhara, M. Kakihana, Y. Haga, M. Hedo, T. Nakama, and Y. Onuki, Unique helical magnetic order and field-induced phase in trillium lattice antiferromagnet EuPtSi, *J. Phys. Soc. Jpn.* **88**, 013702 (2019).
- [44] T. Takeuchi, M. Kakihana, M. Hedo, T. Nakama, and Y. Onuki, Magnetic field versus temperature phase diagram for $H \parallel [001]$ in the trillium lattice antiferromagnet EuPtSi, *J. Phys. Soc. Jpn.* **88**, 053703 (2019).
- [45] T. Kurumaji, T. Nakajima, M. Hirschberger, A. Kikkawa, Y. Yamasaki, H. Sagayama, H. Nakao, Y. Taguchi, T.-h. Arima, and Y. Tokura, Skyrmion lattice with a giant topological Hall effect in a frustrated triangular-lattice magnet, *Science* **365**, 914 (2019).